Optical Properties of Nanostructured Films Grown by Glancing Angle Deposition

Master Thesis

Sophie Hoppenz

Aalborg University
Nanomaterials and Nanophysics

Materials and production
Aalborg University
https://www.mp.aau.dk

AALBORG UNIVERSITY
STUDENT REPORT

Title:
Optical Properties of Nanostructured Films Grown by Glancing Angle Deposition

Theme:
Nanomaterials and Nanophysics

Project Period:
Fall Semester 2022/
Spring Semester 2023

Project Group:
MNNF3/ MNNF4

Participant(s):
Sophie Hoppenz

Supervisor(s):
Kjeld Pedersen

Copies: 1

Page Numbers: 44

Date of Completion:
May 31, 2023

Abstract:

Glancing angle deposition (GLAD) is an easy to implement, one-step method for the growth of nanocolumnar structures by using shadowing effects. These columns can have localized surface plasmon resonance excitations, making them of interest for countless optical applications, amongst others in optical sensing.
In this work, thin films with columnar structures of gold were grown using glancing angle deposition. The gold was deposited on a silicon substrate with a 5 nm thick layer of chromium for increased adhesion.
Both the linear and nonlinear optical properties of the gold nanorods were characterized, measuring their reflectance and the second harmonic generation as a function of the orientation of the nanorods. The experimental results were compared to theoretical models. Besides the dependence on the orientation of the rods, optical properties also showed a strong dependence on the polarization and the angle of the incoming light.

Chapter 1

Summary

Glancing angle deposition is a ballistic deposition technique in which the shadowing effect is used to grow angled nanocolumns. In this thesis work, these columns will be grown and their linear and nonlinear optical response will be investigated.

The nanostructured films were deposited via thermal resistive evaporation. As substrate, silicon wafer pieces were used. The substrates were covered with 5 nm of chromium to increase the adhesion of the columnar structures. The rods themselves were grown with gold.

To investigate the linear optical properties of the gold nanorod structures, the dependence of the reflectance of p-polarized light at an incidence angle of 8° on the wavelength of light was measured along with the orientation of the angled columns in relation to the plane of incidence of the incoming light. To gain new insight into the nonlinear optical behaviour of the structure, the second harmonic generation was measured, again as a function of the orientation of the nanorods. Rotational scans at set wavelengths were performed for different combinations of polarizations of the incoming and outgoing light. To make predictions about the optical behaviour of the angled nanocolumns for both the linear and the nonlinear case, two different preexisting models from literature were used and the results were compared to the experimental data.

The reflectance measurements revealed the presence of different types of surface plasmon resonances on the sample, depending on the orientation of the nanowires. For all cases, a gold bulk plasmon resonance and a localized surface plasmon resonance could be observed. For the rods being rotated out of the plane of incidence, an additional surface plasmon resonance was found. The model used to compare to the experimental results had difficulties predicting the optical behaviour beyond some characteristic points, as it fails to take several important properties of the investigated samples, such as the multi-layered substrate or the inhomogeneity of the columns, into account.

Measuring second harmonic generation confirmed the existence of localized

surface plasmon resonances found in the reflectance measurements. They were found to be the strongest in the transversal mode. These experiments revealed the presence of cross-polarization as well. The model adopted from literature was developed using a symmetry similar in nature to the symmetry of the nanocolumn layer developed in this thesis work. While reliable qualitative predictions about the locations of the maxima and minima in second harmonic generations could be made as long as no cross-polarization was present, the difference in the symmetry of the two structures proved to be too strong for the model to make reliable predictions when cross-polarization had to be taken into account.

Both the linear and the non-linear optical responses of the nanocolumn films grown in this thesis show strong dependence on the polarization and the angle of the incoming light, as well as on the orientation of the wires relative to the plane of incidence of the incoming light. Glancing angle deposition is thus a powerful technique for engineering of optical properties of thin films.

Contents

Preface

This master thesis was written by group Sophie Hoppenz, a 4th semester student of the Master's program Nanomaterials and Nanophysics at Aalborg University, supervised by Kjeld Pedersen. The project lasted from the 2nd of September 2022 to the 1st of June 2023. The author would like to thank my supervisor Kjeld Pedersen for his guidance and feedback. Furthermore, the author would like to thank Peter Kjær Kristensen and Deyong Wang for their help in the cleanroom.

The numerical modelling and plots were done using Matlab. Figures were created using Inkscape. The thesis work was written using LaTeX in Overleaf.

Aalborg University, May 31, 2023

Sophie Hoppenz
<shoppe21@student.aau.dk>

Chapter 2

Introduction

Glancing angled deposition (GLAD) is an important tool for the fabrication of nanostructured films that has been of interest for over 100 years. It is a ballistic deposition method that uses shadowing mechanisms for the formation of columnar structures. The growth of these structures is a one-step process, which is easy to implement, fast and cost-effective [2, 1]. This makes GLAD a far superior method for the growth of nanocolumns compared to other commonly used techniques, such as e-beam lithography. Nanostructured films deposited using GLAD have applications in a variety of different fields, such as energy harvesting and storage where they can for example be used in photovoltaic cells, or sensor devices, such as pressure or humidity sensors.

They can also be used in optical sensors, as their optical response is highly sensitive to their surroundings. This is due to the localized surface plasmons present in the wires. Optical sensors using surface plasmon resonance are able to measure small changes in the the refractive index of the surrounding medium fast and precisely. Nanowires can help enhance this effect, as the localized surface plasmon resonance enhances the electric field around the nanocolumns, resulting in a higher sensitivity.

The angled orientation of the nanowires ensures that the medium exhibits anisotropic behaviour - meaning the optical response depends on the direction and polarization of the incoming light. Both the angle to the nanocolumns relative to the substrate and the angle of the incoming light to the substrate influence the optical response of the material.

This can be seen in the second harmonic generation these nanotructured films exhibit, which will be investigated experimentally in this thesis. Second harmonic generation is a nonlinear optical process where incident monochromatic light at a frequency ω generates light at twice the frequency 2ω. The second harmonic generation in anisotropic media has previously been investigated in literature and yields an angle-dependent intensity [3, 8].

Just like the experimental results for the nonlinear optical investigations, the linear optical experiments will be compared to previously used models from literature as well. Here, an effective medium approach can be used, as the columns are structured as an optical metamaterial. In optical metamaterials, the sizes of their individual structures and the distances between them have to be much smaller than the investigated wavelength. Then their electromagnetic response can be expressed in terms of parameters of the whole material. This approach will be used to model the optical response of the nanorod layer [4, 2, 18, 1].

The aim of this thesis is to grow angled nanorods using glancing angle deposition and to investigate their linear and nonlinear optical properties. More specifically, the structures examined in this work are angled gold nanorods deposited on silicon substrates with a 5 nm layer of chromium to increase adhesion [1]. To gain a deeper insight into their optical behaviour, their reflectance and second harmonic generation are both measured and modeled using previously developed methods from literature.

Chapter 3

Glancing Angle Deposition

3.1 Principles of glancing angle deposition

Glancing angle deposition (GLAD) is a thin film fabrication method, during which the incoming vapor flux of particles arrives at the substrate surface at an oblique angle. The material is typically deposited through physical vapor deposition using evaporation. More specifically, in this work resistive evaporation under vacuum was used. In the beginning of the deposition, initial nuclei will either form on the substrate surface at random or will already be present. The latter could be the case either due to random inhomogeneities on the substrate or a previously fabricated pattern. The continuously incoming stream of particles will then be prevented from reaching the regions behind these nuclei, resulting in a so called shadowing effect. As the deposition continues, this effect will be amplified, resulting in the growth of tilted columns [2]. The effect is illustrated in figure 3.1. The deposition angle α relative to the surface normal is indicated in figure 3.1. It dictates the length of the shadowed region via $h \cdot tan(\alpha)$. If α increases, so does the shadowed area on the substrate. For angles above 85°, the shadow length becomes larger than the diffusion length, such that it dominates the deposition. This results in a columnar growth and a reduced film density. The column tilt angle β, indicated in figure 3.1b as well, points in the direction of the incoming vapor flux, but will always be less than α. Predictions about it can be made using Tait rule:

$$\beta = \alpha - arcsin(\frac{1 - cos(\alpha)}{2}) \tag{3.1}$$

Even though Tait rule delivers values in high agreement with what was observed in experiments, it is only a geometric analysis of intercolumnar shadowing effects. Therefore, it does not take growth kinetics into account. Several other factors, such as deposition rate and substrate temperature, have an influence on the final column tilt angle. Several different more advanced models exist, which have fitting

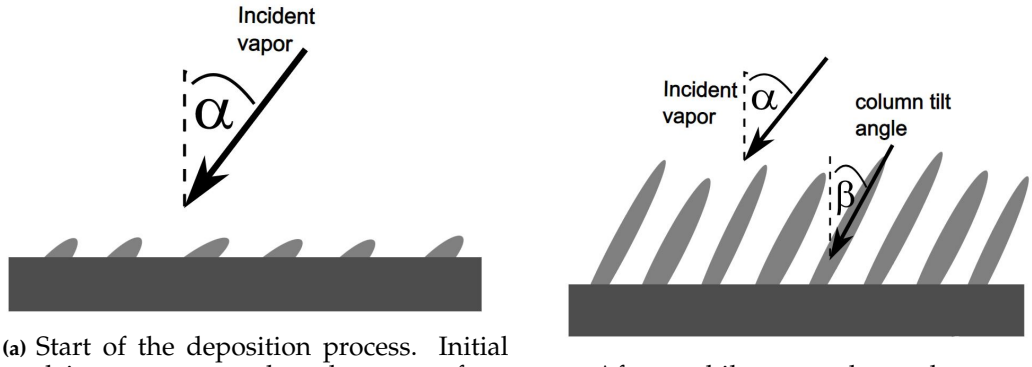

(a) Start of the deposition process. Initial nuclei are present on the substrate surface. The vapor flux arrives at an angle α relative to the surface normal.

(b) After a while, nanocolumns have grown on the surface. β is their columnar tilt angle relative to the surface normal.

Figure 3.1: GLAD process at the beginning and during the deposition.Inspired by [16], p. 624, Figure 13.2.

parameters and can be tailored specifically to experimental data of the deposited material, but Tait rule can function as a reliable first estimate [16, 6].

The requirement for these tilted columns to grow is that the incoming atoms are incorporated into the structure where they hit the substrate, which is referred to as ballistic deposition. This is only the case if the diffusion of adatoms on the substrate surface is low. The surface diffusion of the adatoms depends mainly on two parameters, the surface temperature and the deposition rate. Higher deposition rates give less time to diffusion processes on the surface and the incoming flux of particles buries particles on the surface before they can diffuse. Therefore, the deposition rate has to be sufficiently high for nanocolumns to grow. To limit thermally activated diffusion processes, the temperature on the substrate has to be kept low. For glancing angle deposition to result in columnar growth, the deposition should take place in zone I of the Movchan and Demchishin structure zone model [2, 16].

This model describes the properties of the thin film in relation to the homologous temperature T_h, which is given by the ratio between the substrate surface temperature T and the melting point of the deposited material T_m. The structures are then divided into three zones. Zone I is in the range of $T_h \leq 0,3$. The resulting thin film has very small Crystallinities with high defect density, surrounded by void boundaries. A columnar structure grows due to insufficient diffusion. As T_h increases in zone II and III, the density and with it the number of defects in between the columns increase as well. In zone III, the thin film is made up of coarse grains. Therefore, glancing angle deposition needs to be conducted in zone I of the Movchan and Demchishin structure zone model, such that the desired columnar structures can be obtained and the diffusion of the adatoms into the shadowed

regions behind the grains is limited [12, 2].

Throughout the deposition, the structure of the nanopillars begins to deviate more and more from the previously described ideal form. As the columns grow, some will do so faster than others. The slower growing columns might fall into the shadow of the larger ones, such that they can not continue to grow. This is referred to as column extinction. The process is illustrated in figure 3.2.

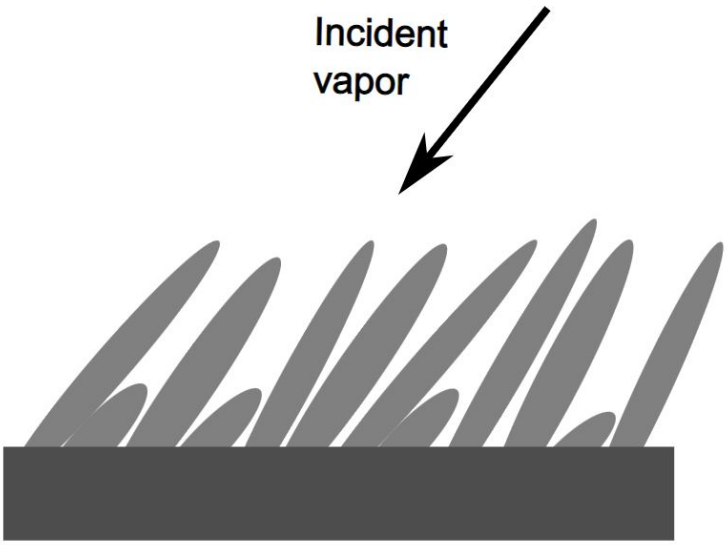

Figure 3.2: The slower growing columns have fallen into the shadow of the larger ones and can not continue to grow. This is referred to as column extinction. Inspired by [16], p. 624, Figure 13.2.

The shadow effect can also influence the structure of a singular column. As the column surfaces are not homogeneous, the shadowing effect will cause them to roughen further, which causes the columns to broaden as they grow and even split into sub-columns. This effect is called bifurcation. It is counteracted by lateral diffusion and can therefore be influenced by the substrate temperature. The effect is more pronounced in wider and bigger columns, as their internal structures are bigger. While the depositing angle α does not seem to have a clear influence on the broadening of the columns, a clear relation to the substrate temperature is apparent. The increase in width happens faster at higher temperatures [6, 16].

3.2 Applications

Nanostructured films deposited using glancing angle deposition have many applications in the field of optical sensing, as their refractive index and their overall optical response depend strongly on the medium they are in. This is due to the localized surface plasmons - the collective oscillation of free electrons in a nanos-

tructured metal - which will be explained in greater detail in chapter 4.1. They enhance the electric field around the nanocolumns, resulting in a higher sensitivity [2, 1].

The localized surface plasmon resonance depends on the size and shape of the nanocolumns as well as on their surrounding environment. For applications, these films are typically composed of silver or gold. Their response to their surroundings can be further tuned by changing their structure and composition along the axis of the rods. One example this can be used for is to create a varying refractive index along the film thickness to create antireflection coating. For these applications, GLAD has the advantage that it allows a direct control of the composition and shape of the grown structures.

GLAD nanostructured films have many other uses beyond their applications in sensing. The increased electric field due to localized surface plasmon resonance can also be used for metal enhanced fluorescence, where fluorescent particles exhibit an increased emission intensity when they are around metal nanostructures. When luminescent materials are deposited using GLAD, the tilted orientation of the resulting nanocolumns results in a linear polarization of the luminescent emission [2].

Chapter 4

GLAD structures as optical metamaterials

Optical metamaterials are materials that have an artificial structure, which influences their optical responses. The sizes of their individual structures and the distances between them have to be much smaller than the wavelength of interest. When this is the case, the behaviour of these materials is governed by the whole structure, not the singular components, and their electromagnetic response can be expressed in terms of parameters of the whole material. This chapter will focus on the properties of metals as metamaterials. Structuring metals as metamaterials makes them available for a wide range of optical applications, amongst others in the field of sensing using localised surface plasmon resonance. Some of these applications were discussed in section 3.2 [4, 2, 1].

4.1 Surface plasmon resonance

Plasmonics addresses the localization and propagation of light on a subwavelength scale. Exposed to light at optical frequencies, the free electrons in a metal are excited into collective oscillations, called plasmons. When the frequency of the incident light matches the intrinsic frequency of the free electrons, a resonance absorption happens. The surface charge density oscillations of the free electrons in metals are referred to as surface plasmons, and their excitation as surface plasmon resonance. These plasmons can not be excited in single planar interfaces without complicated experimental setups. However, localised surface plasmons are characteristic for interactions between metal nanoparticles and light at optical frequencies, where their excitation is more easily possible.

Regarding a free electron gas that is confined all three dimensions in the shape of a small particle, the electrons will be displaced relatively to the positively charged lattice, which results in a restoring force. This force will then in turn result in an

oscillation that is a particle-plasmon resonance, which will be characteristic to the geometry of the particle. If the particles are suitably shaped, typically meaning they are pointy, localized charge accumulations can occur. These accumulations are then accompanied by strongly enhanced optical fields. When these surface plasmons are present at a metal dielectric interface, they can result in strongly enhanced optical near-fields that are spatially confined to the near metal surface [13, 2].

One form these metal nanoparticles can take is nanorods grown by glancing angle deposition like the ones described in chapter 3. The rods will then have two different modes of localised surface plasmon resonance, one for polarization along the axis of the rods (longitudinal mode *LM*) and one for polarization perpendicular to the rods (transverse mode *TM*). If the aspect ratio of the pillars is high enough, the resonance wavelengths for these two modes will be clearly distinguishable. One of the two can then be chosen by choosing the polarization of the incoming light. The wavelength of the localised surface plasmon resonance can also be influenced by the distance between the individual rods, as localized plasmon fields can couple when they get close enough together, which influences the wavelength [18].

4.2 The reflection coefficient

The reflection coefficient describes the fraction of the energy reflected when an incoming plane wave of light hits an interface, while the transmission coefficient is the fraction of the energy transmitted through the interface into the sample. The light in this case can be described as a plane harmonic wave in the shape of:

$$\vec{E}(\vec{r},t) = \vec{E_0} e^{i(\vec{k}\cdot\vec{r}-\omega t)} \tag{4.1}$$

where $\vec{k}$ is the wave vector, ω is the angular frequency and $\vec{E_0}$ is the amplitude of the incoming field and determines the polarization. The corresponding magnetic field is perpendicular to this electric field and can be found through Maxwell's equations. This general plane harmonic wave can be described as a combination of two parts. The first part consists of the electric field that is perpendicular to the plane of incidence and parallel to the interface is referred to as s-polarized light. The second part consists of an electric field that is parallel to the plane of incidence and perpendicular to the direction of light is the p-polarized light[14].

The reflection coefficients can then be found using boundary conditions at the interface. Both the components of the electric field and the magnetic field that are parallel to the surface have to be continuous at the surface, which leads to the following equations for the reflection coefficient for s-polarized light r_s and the one

for p-polarized light r_p:

$$r_s = \frac{n_i \cos(\theta_i) - n_t \cos(\theta_t)}{n_i \cos(\theta_i) + n_t \cos(\theta_t)} \tag{4.2}$$

$$r_p = \frac{n_i \cos(\theta_t) - n_t \cos(\theta_i)}{n_t \cos(\theta_i) + n_i \cos(\theta_t)} \tag{4.3}$$

In the same way, the equations for the transmission coefficients for s-polarized light t_s and for p-polarized t_p light can be found:

$$t_s = \frac{2n_i \cos(\theta_i)}{n_i \cos(\theta_i) + n_t \cos(\theta_t)} \tag{4.4}$$

$$t_p = \frac{2n_i \cos(\theta_i)}{n_i \cos(\theta_t) + n_t \cos(\theta_i)} \tag{4.5}$$

In these equations, n_i and n_t are the refractive indices of medium i and medium t, respectively, where the direction of the incoming light is from medium i[14]. n_t can be found through its relation to the dielectric function ϵ_r and the permeability μ_r [7]:

$$n_t = \sqrt{\epsilon_r \cdot \mu_r} \tag{4.6}$$

θ_i is the angle of incidence of the light and θ_t is the angle of the transmitted light, which can be found using Snell's law:

$$n_i \sin(\theta_i) = n_t \sin(\theta_t) \tag{4.7}$$

The reflectance R is the fraction of the power in the incidence wave that is reflected, it can be calculated using the following equation [14]:

$$R = \mid r \mid^2 \tag{4.8}$$

4.3 The optical response of metals

4.3.1 The Drude-Lorentz model

A simple model for the dielectric function for metals, which was mentioned in the previous section, can be found by considering the electrons which can move freely in the lattice of a metal. The electrons can be described by a Lorentz harmonic oscillator model, with no forces acting on the electrons. The resonance frequency ω_0, which is the oscillation frequency of electrons under an applied electric potential, is zero. This leads to the Drude free electron model for the dielectric function:

$$\epsilon(\omega) = 1 - \frac{\omega_p^2}{\omega^2 + i\Gamma\omega} \tag{4.9}$$

where ω is the frequency. Γ is the damping constant, that is proportional to the electron collision rate. The plasma frequency ω_p depends on the density of free electrons in the metal n, the elementary charge e, the electron mass m_e and the vacuum permittivity ϵ_0:

$$\omega_p = \sqrt{\frac{ne^2}{\epsilon_0 m_e}} \tag{4.10}$$

To take the contribution from bound electrons into account in the Drude model, a constant factor ϵ_∞ can be added, bringing the dielectric function into the following form:

$$\epsilon(\omega) = \epsilon_\infty - \frac{\omega_p^2}{\omega^2 + i\Gamma\omega} \tag{4.11}$$

The constant ϵ_∞ is derived from experimental data. For wavelengths that are much higher than the wavelengths of the interband transitions, almost all light is reflected. At low wavelengths, the optical response of the metal is dominated by the interband transition. In the case of gold, this results in low reflectance at low wavelengths [4]. When a fit is made using experimental data obtained by Johnson et al. in their article *Optical constants of the noble metals* [10], the following values can be found for gold: $\epsilon_\infty = 9$, $\hbar\omega_p = 9.1$ eV and $\hbar\Gamma = 0.072$ eV [4].

The contribution from bound electrons can also be taken into account in a more rigorous manner. The Drude free electron model only takes the electrons of the outer atomic orbital into account. For gold this is the 6s orbital. The Drude-Lorentz model also includes interband transitions, such as the transition from 5s to 6sp for gold. This interband contribution is given by:

$$\epsilon_{ib} = 1 + \frac{\omega_1^2}{\omega_0^2 - \omega^2 - i\gamma\omega} \tag{4.12}$$

where γ is the damping constant of bound electrons, ω_0 is the resonance frequency, and ω_1 is proportional the density of bound electrons. To arrive at the Drude-Lorentz model, this interband contribution is added to the Drude free electron model [4]:

$$\epsilon(\omega) = \epsilon_{ib}(\omega) + 1 - \frac{\omega_p^2}{\omega^2 + i\Gamma\omega} \tag{4.13}$$

A fit for gold is made using the parameters mentioned above for gold for the intraband contribution as well as $\hbar\omega_1 = 3$ eV, $\hbar\gamma = 0.6$ eV and $\hbar\omega_0 = 2.8$ eV [4].

For a more accurate model, more Drude-Lorentz terms can be added, with each new term corresponding to an interband transition, leading to the following expression:

$$\epsilon_{DL}(\omega) = \epsilon_{\infty,DL} - \sum_{i=1}^{NDL} \frac{A_i^2}{\omega^2 - \omega_i^2 + i\Gamma_i\omega} \tag{4.14}$$

$\hbar A_i$ [eV]	8.31	3.28	3.31	4.8	10.4
$\hbar\omega_i$ [eV]	0.265	3.00	3.90	4.65	7.71
$\hbar\Gamma_i$ [eV]	0.0655	0.904	1.22	1.89	4.66

Table 4.1: Parameters for fitting the gold dielectric function to the experimental data from[10], calculated in [5]. Besides the parameters in the table $\epsilon_{\infty,DL} = 1.87$ is needed for the gold-fit.

NDL is the number of Drude-Lorentz terms that is used, in this case it will be five. A_i is the amplitude and a product between the squared plasma frequency and the oscillator strength. ω_i is the respective resonance frequency of the term. Γ_i is the damping coefficient, which governs the broadening of the resonance peaks. A_i, ω_i and Γ_i are in eV. The values for these constants are listed in table 4.1 for gold. This approach will be used in chapter 7.1.2 [5].

4.3.2 Effective medium theory

Effective medium theory uses the homogenization of an inhomogeneous medium with different components. For this approach to be valid, the investigated structures need to be large enough to keep their individual electromagnetic behaviour, but small enough for the medium to appear macroscopically homogeneous. In this work, the approach that Yanfeng Wang et. al. used in their paper "The IR plasmonic properties of subwavelength ITO rod arrays predicted by anisotropic effective medium theory" will be replicated [18].

In their work, Wang et.al. describe the path of the incoming light to go from medium 1, air with the dielectric function ϵ_1, onto the surface of medium 2 under an angle of θ relative to the surface normal of medium 2. Medium 2 is composed of nanorods. These are described as an effective medium layer. Below medium 2, there is medium 3; an optically anisotropic and semi-infinite layer. Both the nanorods and the incident plane of the light are in the xz-plane. The structure is illustrated in figure 4.1 [18].

The relevant parameters of the film are the height of the pillars l, the tilt angle of the pillars relative to the surface normal β, the diameter of the pillars w and the distance d between them. The dielectric tensor of the nanorod layer can be defined in according to the coordinate system of the rods as:

$$\begin{pmatrix} \epsilon_{x'} & 0 & 0 \\ 0 & \epsilon_{y'} & 0 \\ 0 & 0 & \epsilon_{z'} \end{pmatrix} \tag{4.15}$$

where x', y' and z' are the axes of the nanorod directions as can be seen in figure 4.1. The nanorod structure only has one optical axis, the z' axis [18]. This leads to

$$\epsilon_{x'} = \epsilon_{y'} \neq \epsilon_{z'} \tag{4.16}$$

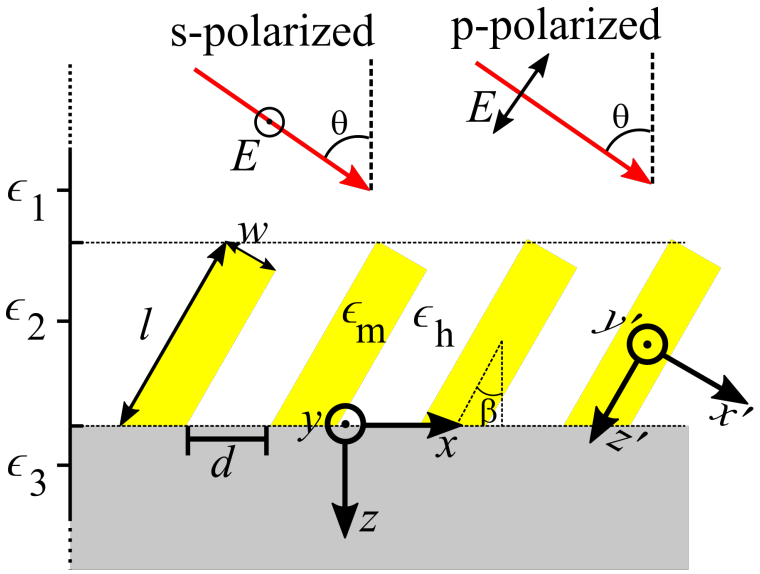

Figure 4.1: A schematic of the model with three media; a semi-infinite substrate, angled nanorods and air. The incoming light for the p- and s-polarized case is indicated as well as both the axes of the sample and the wires. Inspired by [18], p. 2, figure 1.

Then, $\epsilon_{z'}$ has to be found, as it is the effective dielectric function ϵ_{eff} of the layer in the relevant direction. This can be done with the following equation:

$$\frac{\epsilon_{eff} - \epsilon_h}{\epsilon_h + g_j(\epsilon_{eff} - \epsilon_h)} = f_{rods}\frac{\epsilon_m - \epsilon_h}{\epsilon_h + g_j(\epsilon_m - \epsilon_h)} \tag{4.17}$$

f_{rods} is the volume filling factor of the rods which here is simply found as $f_{rods} = \frac{\pi(w/2)^2}{(w+d)^2}$. For equation 4.17 to hold, the material with dielectric constant ϵ_h must be the host medium for the rods, meaning that $f_{rods} << 0,5$. The host medium is air. ϵ_m is the dielectric constant of the bulk material that the nanorods are made of. The rods are modeled as elongated ellipsoid with a high aspect ratio, which the geometric factor g_j takes into account. For light polarized parallel to the rods, $g_{z'}$ becomes [18]:

$$g_{z'} = \frac{1-e^2}{e^2}\left(\frac{1}{2e}\ln\left(\frac{1+e}{1-e}\right) - 1\right) \tag{4.18}$$

where $e = \sqrt{1 - (\frac{w}{l})^2}$ is the eccentricity. For perpendicular rods, $g_{x'} = g_{z'}$ becomes:

$$g_{x'} = g_{y'} = \frac{1}{2}(1 - g_{z'}) \tag{4.19}$$

These equations are in the coordinate system of the angled nanorods and need to be transformed into substrate coordinates, which can be done with equation

4.20.

$$\bar{\epsilon}_2 = \begin{pmatrix} \epsilon_{x'}\cos^2\beta + \epsilon_{z'}\sin^2\beta & 0 & (\epsilon_{z'} - \epsilon_{x'})\sin\beta\cos\beta \\ 0 & \epsilon_{x'} & 0 \\ (\epsilon_{z'} - \epsilon_{x'})\sin\beta\cos\beta & 0 & \epsilon_{x'}\cos^2\beta + \epsilon_{z'}\sin^2\beta \end{pmatrix} \tag{4.20}$$

The reflectance for s-polarized light R^s_{123} can be calculated from the reflection coefficient r^s_{123}:

$$R^s_{123} = \mid r^s_{123} \mid^2 \tag{4.21}$$

The generalized reflection coefficient is:

$$r^s_{123} = r^s_{12} + \frac{t^s_{12} r^s_{23} t^s_{21} \exp(2i\varnothing^s)}{1 - r^s_{23} r^s_{21} \exp(2i\varnothing^s)} \tag{4.22}$$

The factor $\varnothing^s$ dependent on the nanorod layer thickness d_2 is $\varnothing^s = \frac{2\pi d_2}{\lambda}\sqrt{\epsilon_{x'} - \epsilon_1 \sin^2(\theta)}$. The Fresnel coefficients in equation 4.22 are defined as:

$$r^s_{mn} = \frac{Y_m - Y_n}{Y_m + Y_n}, \qquad t^s_{mn} = \frac{2Y_m}{Y_m - Y_n} \tag{4.23}$$

where the factors Y_m and Y_n are surface admittances:

$$Y_m = -\frac{k_0}{\omega\mu_0}\sqrt{\epsilon_m - \epsilon_1 \sin^2(\theta)} \tag{4.24}$$

with $k_0 = \omega\sqrt{\frac{1}{\epsilon_0\mu_0}}$.

For p-polarized light, the reflectance R^p_{123} is:

$$R^p_{123} = \mid r^p_{123} \mid^2 \tag{4.25}$$

The generalised reflection coefficient for p-polarized light is:

$$r^p_{123} = r^p_{12} + \frac{t^p_{12} r^p_{23} t^p_{21} \exp[i(\phi^p_+ - \phi^p_-)]}{1 - r^p_{23} r^p_{21} \exp[i(\phi^p_+ - \phi^p_-)]} \tag{4.26}$$

where $\phi^p_\pm$ are the phase angles of the propagating (+) and reflecting (-) wave, which can be calculated using equation 4.27.

$$\phi^p_\pm = \frac{2\pi d_2}{\lambda}\left(\frac{-\epsilon_{xz} n_1 \sin(\theta) \pm \epsilon_{x'}\epsilon_{z'} Z_2 \epsilon_0 c_0}{\epsilon_{zz}}\right), \tag{4.27}$$

with $\epsilon_{xz} = (\epsilon_{z'} - \epsilon_{x'})\sin\beta\cos\beta$ and $\epsilon_{zz} = \epsilon_{x'}\cos^2\beta + \epsilon_{z'}\sin^2\beta$. The transmission and reflection coefficients r^p_{mn} and t^p_{mn} are given by equation 4.28:

$$r^p_{mn} = \frac{Z_m - Z_n}{Z_m + Z_n}, \qquad t^p_{mn} = \frac{2Z_m}{Z_m + Z_n} \tag{4.28}$$

where the surface impedance Z_m is given by equation 4.29 for m = 1, 3

$$Z_m = \frac{\sqrt{k_0^2 \epsilon_m - k_x^2}}{\epsilon_m} = \frac{k_0}{\omega \epsilon_0} \frac{\sqrt{\epsilon_m - \epsilon_1 \sin^2(\theta)}}{\epsilon_m} \tag{4.29}$$

and by equation 4.30 for m = 2.

$$Z_2 = \frac{k_0}{\omega \epsilon_0} \frac{\sqrt{\epsilon_{zz} - \epsilon_1 \sin^2(\theta)}}{\sqrt{\epsilon_{x'} \epsilon_{z'}}} \tag{4.30}$$

with the vacuum wave vector $k_0 = \frac{\omega}{c}$ and the wave vector in the x direction $k_x = k_0 \sqrt{\epsilon_1} \sin\theta$ [18].

Using the equations introduced in this chapter, the optical response of the nanostructured layer grown in this work can be modeled. For this, an appropriate dielectric function for both the nanorods and the substrate has to be chosen. The dimensions of the nanorods have to be taken into account as well.

This theory only takes nanorods into account that are laying in the plane of incidence of the incoming light. The reason for this is that if the system is rotated such that the rods are no longer lying in the plane of incidence, the s- and p-polarized light will be coupled and the theory will have to be amended[15, 11].

Chapter 5

Nonlinear Optics

Nonlinear optics is the effect of the modification of the optical properties of a material by light. Only laser light is strong enough to cause these effects. When an optical field is applied to a material system, it causes a response in the material that depends nonlinearly on the strength of the applied optical field [3].

5.1 Second harmonic generation

The second harmonic generation is the part of the atomic response to light that exhibits a quadratic dependence on the applied field. The intensity of this generated light has a quadratic dependence on the intensity of the incoming laser light as well. The induced polarization $\vec{P}$ can be developed from the linear induced polarization, which has the form:

$$P(t) = \epsilon_0 \chi^{(1)} E(t) \tag{5.1}$$

where ϵ_0 is the vacuum permittivity, $E(t)$ is the electric field and $\chi^{(1)}$ is the linear susceptibility. To get the nonlinear polarization, equation 5.1 can be expressed in a more general form using a power series:

$$P(t) = \epsilon_0(\chi^{(1)} E(t) + \chi^{(2)} E(t)^2 + \chi^{(3)} E(t)^3 + ...) \tag{5.2}$$

where $\chi^{(2)}$ and $\chi^{(3)}$ denote the second and third order nonlinear susceptibilities respectively [3].

The part of equation 5.2 that concerns the second harmonic generation will now be investigated in greater detail, using a laser beam with the electric field E:

$$E = E_0 e^{-i\omega t} + c.c. \tag{5.3}$$

where ω is the frequency, t is the time, c.c. is the complex conjugate of the electric field and E_0 is the amplitude of the electric field. It is assumed that this electric

field is incident on a crystal with $\chi^{(2)} \neq 0$. The polarization is then:

$$P^2(t) = 2\epsilon_0\chi^{(2)}E_0E_0^* + (\epsilon_0\chi^{(2)}E_0^2e^{-i2\omega t} + c.c.) \tag{5.4}$$

It can be seen that the polarization has two components. The first one is constant over time. The second contribution results in a light at a frequency of 2ω. Equation 5.4 comes from the wave equation 5.5.

$$\nabla^2E(t) - \frac{n^2}{c^2}\frac{\partial^2E(t)}{\partial t^2} = \frac{1}{\epsilon_0c^2}\frac{\partial^2P^{NL}(t)}{\partial t^2} \tag{5.5}$$

where n is the refractive index, c is the speed of light in vaccuum and $P^{NL}(t)$ is the polarization from the nonlinear response.

Using both equation 5.4 and 5.5, it can be seen that both the right and the left side of the equation must have the same time dependency. Therefore, it can be concluded that the electric field is dependent on $e^{-i2\omega t}$, meaning that light at a frequency of 2ω is being generated.

The process can be visualized as in figure 5.1. Two photons with a frequency of ω are coming into the material system and one photon with a frequency of 2ω is created in a single quantum mechanical process. The virtual level is the energy of an energy eigenstate of an atom combined with that of one or more photons [3].

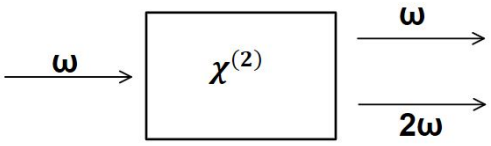

(a) Two incoming photons with the frequency ω create one photon with the frequency 2ω in a single quantum mechanical process.

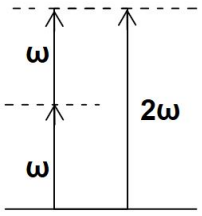

(b) Diagram showing the energy levels. The virtual level is marked by the dashed line, the atomic ground state by the dashed line.

Figure 5.1: Second harmonic generation of light. Inspired by [3], p. 5, figure 1.2.1.

These second harmonic nonlinear interactions only occur in noncentrosymmetric materials, such as the angled nanorods described in chapter 3. The second order polarization resulting from an electric field is given by:

$$P(t) = \epsilon_0\chi^{(2)}E(t)^2 \tag{5.6}$$

where the applied electric field can be described by:

$$E(t) = E_0\cos(\omega t) \tag{5.7}$$

E_0 is the amplitude of the electric field. For a material with centrosymmetry, the equation 5.8 must hold:

$$-P(t) = \epsilon_0 \chi^{(2)}(-E(t))^2 \tag{5.8}$$

This results in:

$$-P(t) = \epsilon_0 \chi^{(2)}(E(t))^2 \tag{5.9}$$

The equations 5.6 and 5.9 can only hold if $\chi^{(2)} = 0$. The average of the polarization $\vec{P}$ for a centrosymmetric medium is zero over time. As a non-centrosymmetric medium responds differently to the electric field pointing in different directions, hence the polarization will not average out to zero over time [3].

5.2 Second harmonic generation in anisotropic media

The nonlinear response of a medium contains information about the symmetry of its interface. This shows in the second harmonic response when the medium is rotated around the surface normal. The rotational anisotropy can be caused by the microtopography of the surface, like it is the case for the angled nanocolumns investigated in this work.

In their paper *Optical second-harmonic generation from vicinal Al (100) crystals*, C. Jakobsen, D. Podenas and K. Pedersen developed a set of equations to describe the second harmonic generation from a surface structured as a regular array of steps. The surface symmetry of this step structure compared to the bulk (100) crystal is reduced to a C_{1v} symmetry, which simplifies the non-linear surface dipole polarization density P^s into [8]:

$$\begin{pmatrix} P_x^s \\ P_y^s \\ P_z^s \end{pmatrix} = \begin{pmatrix} d_{11} & d_{12} & d_{13} & 0 & d_{15} & 0 \\ 0 & 0 & 0 & d_{24} & 0 & d_{26} \\ d_{31} & d_{32} & d_{33} & 0 & d_{35} & 0 \end{pmatrix} \begin{pmatrix} E_x^2 \\ E_y^2 \\ E_z^2 \\ 2E_yE_z \\ 2E_xE_z \\ 2E_xE_y \end{pmatrix}. \tag{5.10}$$

where E_x, E_y and E_z are the linear fields just inside the surface and d_{ij} are the components of the nonlinear susceptibility tensor [3].

From equation 5.10, retaining only the d_{11} tensor element describing the polarizability perpendicular to the steps, they calculated the p- and s-polarized parts of

the second harmonic field that is generated by the stepped medium to be:

$$E^{(2\omega)}(p,p) = (A_{pp} + B_{pp}d_{11}\cos^3\phi)E_p^2, \tag{5.11}$$

$$E^{(2\omega)}(s,s) = B_{ss}d_{11}\sin^3\phi E_s^2, \tag{5.12}$$

$$E^{(2\omega)}(p,s) = B_{ps}d_{11}\sin\phi\cos^2\phi E_p^2, \tag{5.13}$$

$$E^{(2\omega)}(s,p) = (A_{sp} + B_{sp}d_{11}\sin^2\phi\cos\phi)E_s^2 \tag{5.14}$$

The fitting parameters A_{pp}, A_{sp}, B_{pp}, B_{ss}, B_{ps} and B_{sp} depend on the angle of incidence and the refractive index of the investigated medium [8].

It is hypothesized that the nanowires grown in this work, when viewed from the direction of an incoming beam of light, are similar enough to this array of steps for their second harmonic generation to be described by the same set of equations. This hypothesis will be tested in chapter 7.2.

Chapter 6

Setup

6.1 Samples

Figure 6.1 shows a sample with gold nanocolumns grown on a piece of silicon wafer with a layer of 5 nm chromium. The picture was taken using a ZEISS Gemini scanning electron microscope. In order to be able to view the columns from the

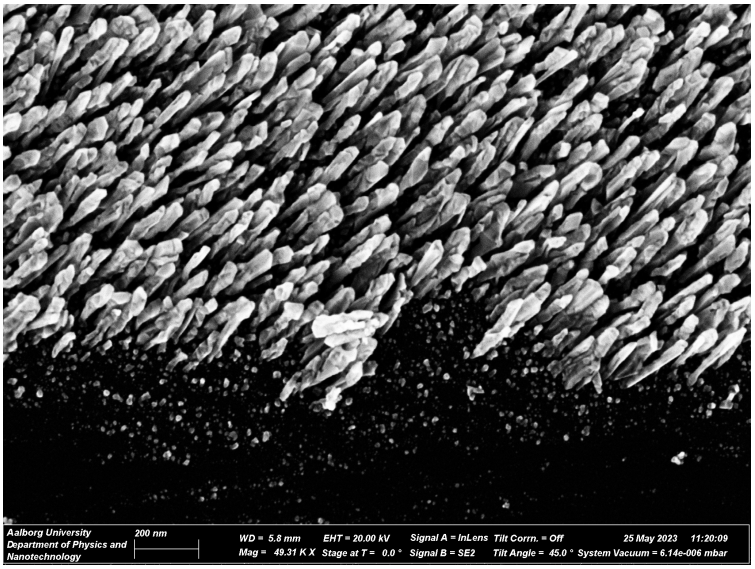

Figure 6.1: Overview of nanocolumns deposited by glancing angle deposition along a scratch on the sample surface.

side, a cut in the structure needs to be made without damaging the columns or changing their configuration. After some trials with different methods, the most effective approach for this proved to be to manually scratch the sample in the growth direction of the nanocolumns. The parameters of the nanostructured film

can be approximated from these pictures, as can be seen from figure 6.2. The

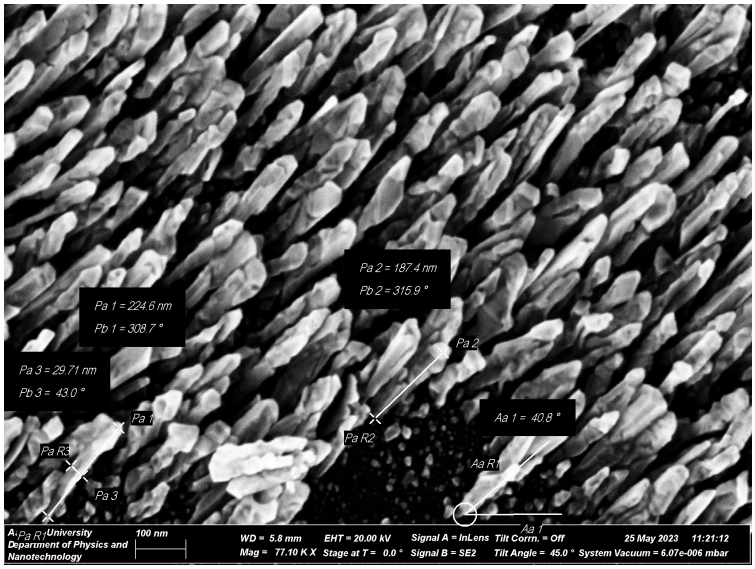

Figure 6.2: Parameters of nanocolumns deposited by glancing angle deposition measured along a scratch on the sample surface.

average height of the columns is approximated as 200 nm, the average width of a single column as 30 nm and the distance between the rods as 40 nm. The average angle between the columns and the substrate is approximated as 40°, making the average columnar tilt angle as defined in chapter 3 50°. From that, the thickness of the layer is approximated as 130 nm.

A sample with a plain gold layer was deposited as well. The deposition chamber from section 6.2 was used with a non-angled substrate holder.

6.2 Glancing Angle Deposition

Figure 6.3 shows the setup used deposit the samples at a glancing angle. As substrates, silicon wafer pieces of two by two centimeters were used. To increase the adhesion of the deposited film, they had a top layer of 5 nm of chromium [1]. The sample is placed on the sample holder, which is angled at 85° relative to the vapor source. Using both a roughening and a turbo pump, a vacuum with a pressure below 10^{-6} mbar is created, before the deposition can be started.

The source material, in this case gold, is located in a crucible under the sample holder. It will be deposited via resistive thermal evaporation. A filament placed around the crucible can be heated up by increasing the current through it. This will melt and evaporate the source material. The vapor rises in the chamber and hits the surface of the substrate, which is located above the crucible at an angle of

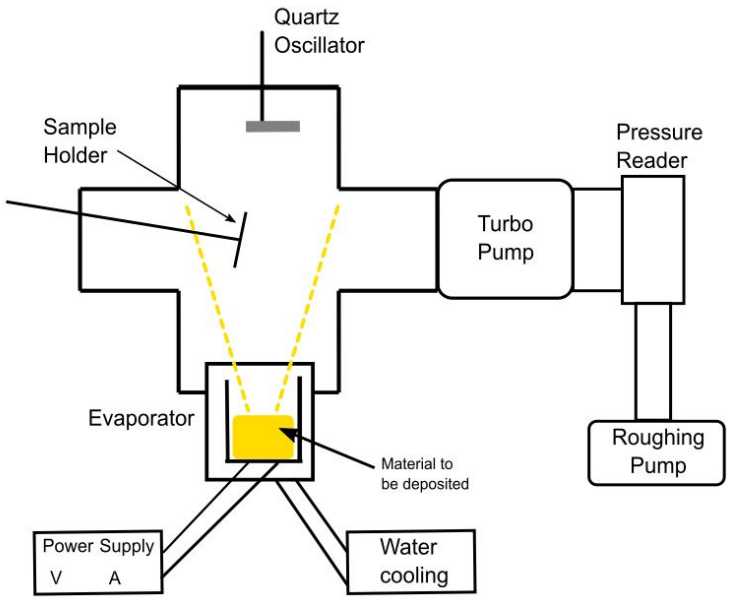

Figure 6.3: Setup used to deposit the angled nanocolumns.

85°.

To monitor the deposition, a quartz oscillator located at the top of the chamber is used. As a part the rising vapor hits the substrate, another part of it will hit the quartz oscillator at the same rate, allowing to monitor both this deposition rate and the film thickness. Once the desired thickness is reached, the deposition can be stopped.

6.3 Reflectivity measurements

The reflectivity measurements were performed using the *PerkinElmer Lambda 1050 UV/VIS/NIR Spectrometer*. Using the program belonging to the machine, *UV WinLab explorer*, the reflectivity in a wavelength range from 250 nm to 2000 nm was measured in steps of 2 nm. The measurements were done with the light hitting the sample at an angle of 8°. A polarizer was inserted to measure with p-polarized light.

6.4 Nonlinear optical measurement

Figure 6.4 shows the setup to measure the nonlinear optical response of the samples. The light is generated by a 5ns pulsed NdYAG laser (Continuum Surelite II-10) with a repetition rate of 10 Hz. The average power of the laser is 10 nW.

It contains a second harmonic generator (SHG), which generates light with a frequency of 2ω and a sum frequency generator (SFG) generating light at a frequency of 3ω. The outgoing beam contains light of the wavelenghts 355 nm, 532 nm and 1064 nm.

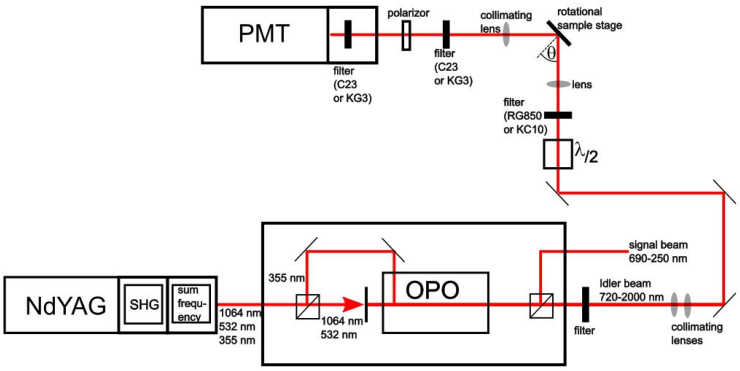

Figure 6.4: Laser setup used for the nonlinear measurements.

The 355 nm light is reflected by a dichroic mirror and directed into the optical parametric oscillator (OPO). The 532 nm and 1064 nm parts hit the OPO as well. The OPO outputs a signal beam of 250 to 690 nm and an idler beam of 720 to 2000 nm, which are separated by a beam splitter. The filter behind the beam splitter removes remaining parts of the signal beam that were not removed by the beam splitter. The idler beam is then focused using collimating lenses to control the beam diameter.

The idler beam is redirected to a half-wave plate without dispersion that can be used to turn the beam into either p-polarized or s-polarized light. A filter is placed behind the half-wave plate to block the parts of the beam corresponding to the second harmonic generation. For wavelengths between 720 nm and 1050 nm, a KC10 filter is used, for wavelengths above 1000 nm it is a RG850 filter. A glass lens with a focal length of 300 mm is used to focus the beam on the sample. The sample is placed on a rotating stage and is hit by the incoming light at an angle of 45°.

The reflected light from the sample is focused in a collimating fused silica lens. It also filters out the UV parts of the incoming beam. Behind this lens, a filter is placed to block light of the pump wavelength and let light of the desired wavelength range pass. For wavelengths between 720 nm and 1050 nm, a C23 filter is used, for 1000 nm to 1400 nm, a KG3 filter is used. A polarizer is placed behind the filter. It can be switched between s- and p-polarization.

The polarized light then hits the photomultiplyer tube (PMT). Here, a PFR 9816 is used. It has a peak power of 0,2 mW. Inside it, an additional C23 and KG3 filter are located as protection from the incoming light.

Four different combinations of polarizations of the incomig and outgoing light are measured; *p to p*, *s to s*, *p to s* and *s to p*.

Both the laser power and the transmission of the optical components depend on the wavelength. Therefore, reference wavelength scans were made using a quartz crystal, as its signal has little dispersion in the wavelength range used in this experiment. The dependence of the second harmonic generation signal from the samples is presented relative to the quartz signal.

Chapter 7

Results

7.1 Reflectance Measurements

The reflectance of the nanostructure grown in this work will be investigated in this chapter. This is done in order to characterize the optical response of the structure. The reflectance measurements will reveal crucial information about the surface plasmon resonances of these films, which plays an important role in a variety of potential applications, as mentioned in chapter 3.2. To develop a model for the nanostructured gold film and investigate its reflectance experimentally, the procedure was first tested with a plain gold layered sample, as this structure has been extensively investigated and the results can easily be compared to theory.

7.1.1 Bulk gold layer

The reflectance of the bulk gold layer sample was measured with the spectrometer described in chapter 6.3. The results are shown in figure 7.1. The characteristic behaviour described in chapter 4.3.1 can be observed. For wavelengths above 900 nm, the reflectance goes towards nearly 100%. For lower wavelengths, the characteristic drop in the reflectance is present.

Figure 7.2a shows the experimental results compared to both the Drude model and the Drude-Lorentz model explained in chapter 4.3.1. Both can not explain the shape of the measurements. It is therefore necessary to employ a more advanced model that uses a better fit to the experimentally obtained constants that are used in these calculations, which are listed in chapter 4.3.

To improve the fit of the Drude-Lorentz model to the experimental results, the form presented in equation 4.14 will be used. It employs more Lorentzians. Figure 7.2b compares the result to the experimental data. This improved model manages to make accurate predictions about the decrease in reflectance.

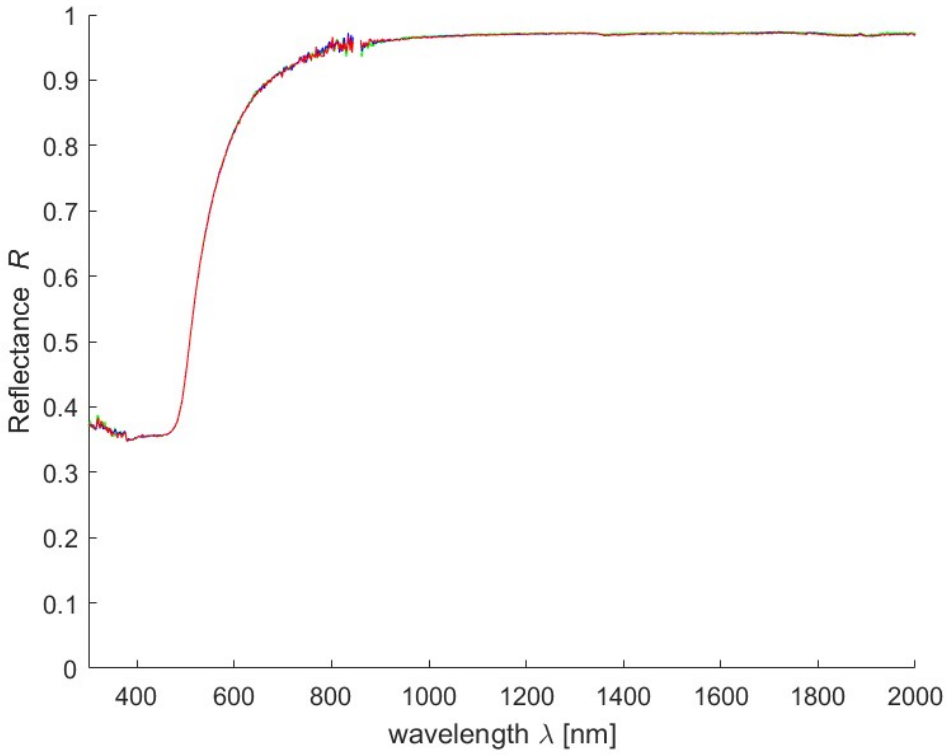

Figure 7.1: Reflectance of the plain gold sample at four different positions on the sample measured at wavelengths between 2000 nm and 300 nm. Around 850 nm, a peak that is caused by a change in grating in the spectrometer was removed.

7.1.2 Angled nanorods

The reflectance of the nanorod layer as a function of the incoming wavelength was measured with the spectrometer described in chapter 6.3. The sample was measured with the rods pointing up, down, left and right and the light coming in at an angle of 8° in the plane horizontal to the sample. The results can be seen in figure 7.3. For all four sample orientations, a minimum around 400 nm can be observed. This is the bulk plasmon resonance of gold, which could also be observed for the bulk gold layer. The minima present at higher wavelengths are localized surface plasmon resonances from the nanorods.

For the wires pointing up and down, a minimum is observed around 600 nm. This is in the range of the surface plasmon resonance for gold [17]. Around 1050 nm, there is a bent in the curve, which could possibly be a localized surface plasmon resonance. In this orientation, the wires are mostly orthogonal to the electric field component of the incoming p-polarized light. This means that the bent around 1050 nm is most likely localized surface plasmons being excited in the

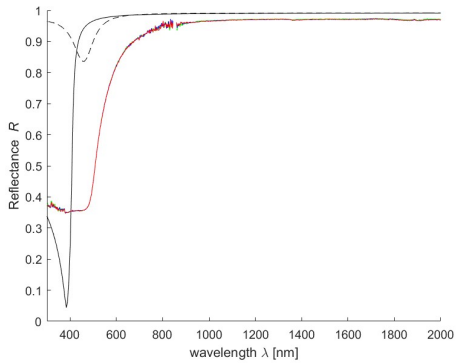

(a) Reflectance of the plain gold sample (colored lines) compared to the Drude-Lorentz model (solid black line) and the Drude model (dashed black line).

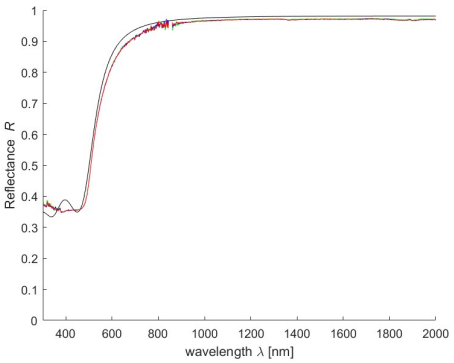

(b) Reflectance of the plain gold sample (colored lines) compared to the 5 terms Drude-Lorentz model (black line).

Figure 7.2: Reflectance of the plain gold sample measured at wavelengths between 2000 nm and 300 nm and different models.

transversal mode *TM* and that the longitudinal mode *LM* can not be observed. This will be confirmed in the next section when the nonlinear optical response is investigated.

When the nanorods are measured while pointing left and right, only one more minimum around 1030 nm can be observed in addition to the one from the bulk plasmon resonance. This minimum coincides approximately with the bent that could be observed for the wires pointing up or down. Considering the orientation of the wires relative to the electric field component while the wires are rotated to the left or right, it can be hypothesized that at 1030 nm, both localized surface plasmon resonances in the longitudinal mode and in the transversal mode are present, as they are rotated into the plane in which the light propagates.

The surface plasmon resonance at 600 nm can not be observed for the wires pointing to the sides. It is unclear why this is the case. Further experiments using s-polarized light and angles of incidence higher than 8° would be necessary to investigate the reasons behind this behaviour.

The model explained in chapter 4.3.2 is then used to describe the experimental results. The measured sample, which is described in chapter 6.1 in greater detail, is a piece of silicon wafer with a 5 nm layer of chromium on which angled nanocolumns were deposited. As can be seen in the figures 6.1 and 6.2, column extinction seems to have taken place in the early stages of the deposition, as many particles and short rods can be seen between the fully grown columns. To take this into account when modeling the nanorod layer and its substrate, it is hypothesized that it is a more accurate approximation to treat these small particles as a thin gold layer on which the rods are grown than to assume that no gold is present between

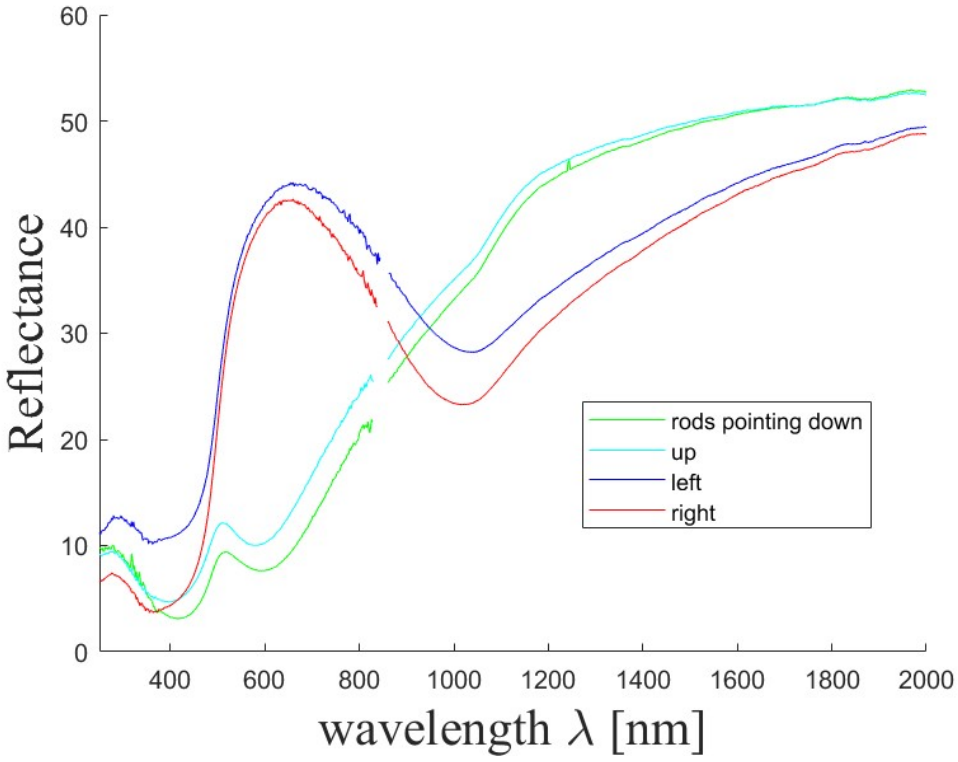

Figure 7.3: The reflectance of the nanorod layer with the rods pointing up, down, left and right. Both bulk plasmon resonance and localized surface plasmon resonances can be observed for all four orientations.

the singular rods. The nanorod layer is then modeled using the approach from chapter 4.3.2. Three different substrates will be investigated in this chapter. As the model uses a semi-infinite substrate, silicon, chromium and gold will be modeled separately, treating each as semi-infinite. For the silicon substrate, the required dielectric function and its parameters were provided by Professor Kjeld Pedersen. For chromium, a typical dielectric constant of $\epsilon_{Cr} = -0.57 + i21.2$ was used, where the dispersion was neglected for simplicity[9]. For the model, the height of the columns is assumed as 200 nm and the width as 30 nm. The columnar tilt angle is 50°. The thickness of the layer is 130 nm and the average distance between the columns is 40 nm. The process to obtain these parameters is discussed in chapter 6.1.

Figure 7.4 shows the results of the reflectance measurements for the wires pointing left and right, meaning that they are in the plane of incidence, compared to the model with the three different substrates.

None of the three cases provide an accurate and quantitative description of the experimental results over the whole measured range. All three curves show

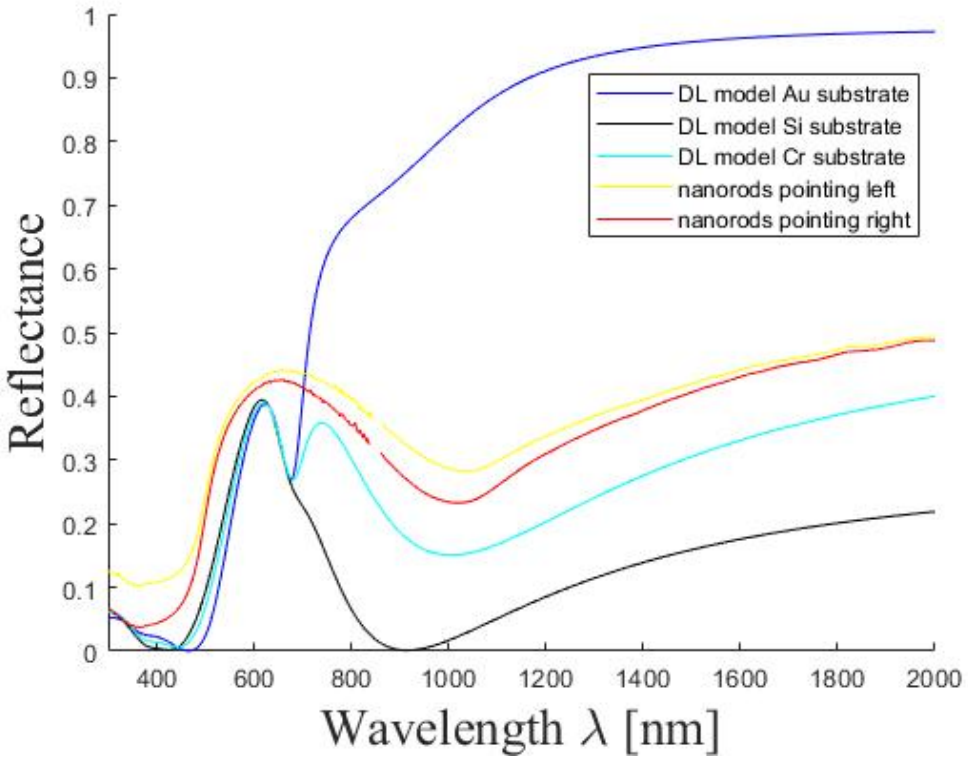

Figure 7.4: The reflectance of the nanorod layer with the rods being in the plane of incidence compared to the model using p-polarized light.

the characteristic bulk plasmon resonance around 450 nm. The results using the chromium and gold substrate exhibit a local minimum around 700 nm, which is not present in the experimental data. This indicates that the model does not accurately describe the system when using these substrates. The silicon and chromium curves have a minimum around 900 nm and 1000 nm respectively. This corresponds roughly to the resonance in the experimental data around 1050 nm. A slight bent in the gold substrate model around 900 nm can be observed, which is suspected to be caused by the same resonance. At high wavelengths, the curve calculated using the gold substrate gets close to complete reflectance, while both silicon and chromium predict too low values for the reflectance for higher wavelengths. This indicates that the gold between the singular rods has an influence on the optical response of the nanorods. A more accurate model would therefore need to take this intercolumnar gold into account.

All three modeled substrates portray some of the characteristic behaviours of the experimental results. Modeling a three layered substrate under the nanorods with a thin layer of gold, followed by a 5 nm layer of chromium and a semi-infinite

layer of silicon can therefore be expected to result in a more precise prediction of the reflectance of the nanocolumn structure. This model was not implemented due to time constraints.

When the sample is rotated such that the wires point up or down, they are not in the plane of incidence anymore, causing the model to break down. For light that is normal to the surface, this rotation of the sample can be implemented in the model by using s-polarized light instead of p-polarized light. Since the light hits the sample at an angle that is only 8° off from this case, it can be hypothesized that the influence of this additional angle is small and the model should still be able to make accurate predictions using s-polarization. Figure 7.5 shows the experimental results for the rods being rotated out of the plane of incidence such that they are pointing up or down, as well as the predictions made by the model when using s-polarized light and the three different substrates.

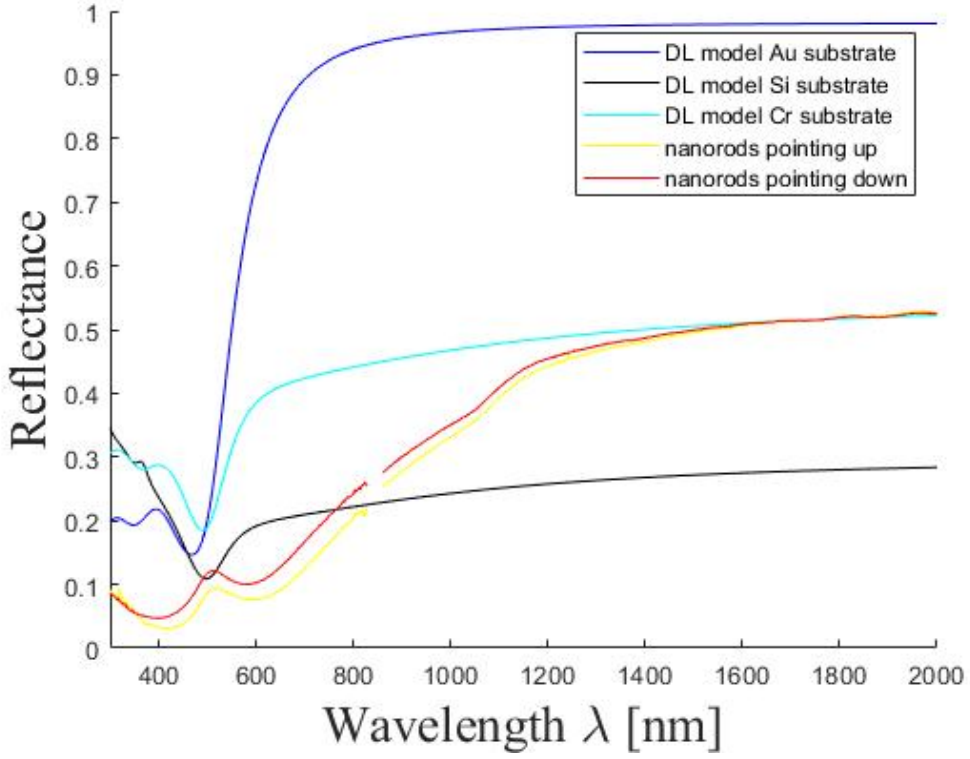

Figure 7.5: The reflectance of the nanorod layer with the rods rotated out of the plane of incidence compared to the model using s-polarized light.

All three versions of the model with the different substrates predict the bulk resonance, similar to the model using p-polarized light. At wavelengths slightly below the one of the bulk resonance, a minimum can be seen in all three curves.

They lay between the bulk plasmon resonance and suspected surface plasmon resonance around 600 nm of the experimental data. These minima might correspond to the resonance at 600 nm in the experimental results, but are shifted towards lower wavelengths. All three cases of the model fail to make accurate predictions concerning the bent in the experimental data around 1050 nm, which could be due to the calculations neglecting the 8° angle of incidence of the light. Including this angle in the model might lead to the minimum seen in Figure 7.4 becoming visible for these orientations of the nanorods as well. This could be a reason behind the bent in the experimental data.

The model fails to make accurate predictions about the reflectance when the nanorods are rotated out of the plane of incidence. Just like in the case of p-polarized light, the accuracy of the model could be significantly increased by implementing the three-layered substrate. Nevertheless, the characteristic properties of the experimental data can not be predicted by the model for the wires being rotated out of the plane of incidence. This seems to disprove the hypothesis, that the influence of the 8° angle on the reflectance is negligible. When the nanocolumns are rotated out of the plane of incidence, the model breaks down. To take the effect of the incidence angle into account, the reflection coefficients would need to be recalculated. This was not implemented due to time constraints.

While each of the models manage to predict some of the characteristics of the reflectance in the case of the nanorods being in the plane of incidence, the overall behaviour can not be accurately predicted. This is even more the case for the nanorods being rotated out of the plane of incidence. One approach to make the models more precise would be to implement the tree layer substrate. The irregularities of the sample have a strong influence on the experimental results as well. If the incoming light used to measure the reflectance hits a defect on the sample surface, this will affect the reflectance. Furthermore, the columns themselves have irregularities. They exhibit column extinction, broadening and bifurcation. These effects will cause the uncertainty of the nanorod layer parameters used in the codes - their length, distance, width, etc. - to increase. As these parameters have a strong influence on the predictions the model makes, this will result in a further deviation of the results predicted by the model from the experimental results.

7.2 Second Harmonic Generation

The measurements to investigate the second harmonic generations were performed using the setup described in chapter 6.4. With the filters used in the setup, the only light that passes through them is the one resulting from the second harmonic generation.

On the sample shown in chapter 6.1, a wavelength sweep from 720 to 1400 nm was performed while both polarizors were set to p-polarization. The light used

in these measurements hits the sample at an angle of 45°. This was done to find the wavelength at which the highest second harmonic generation can be measured. Figure 7.6 shows the recorded spectrum. The maximum can be found at 1028 nm. This coincides approximately with the plasmon resonance wavelength observed from the reflectance spectra in chapter 7.1, but could also be due to a possible resonance at the wavelength of the second harmonic generation, which is 514 nm.

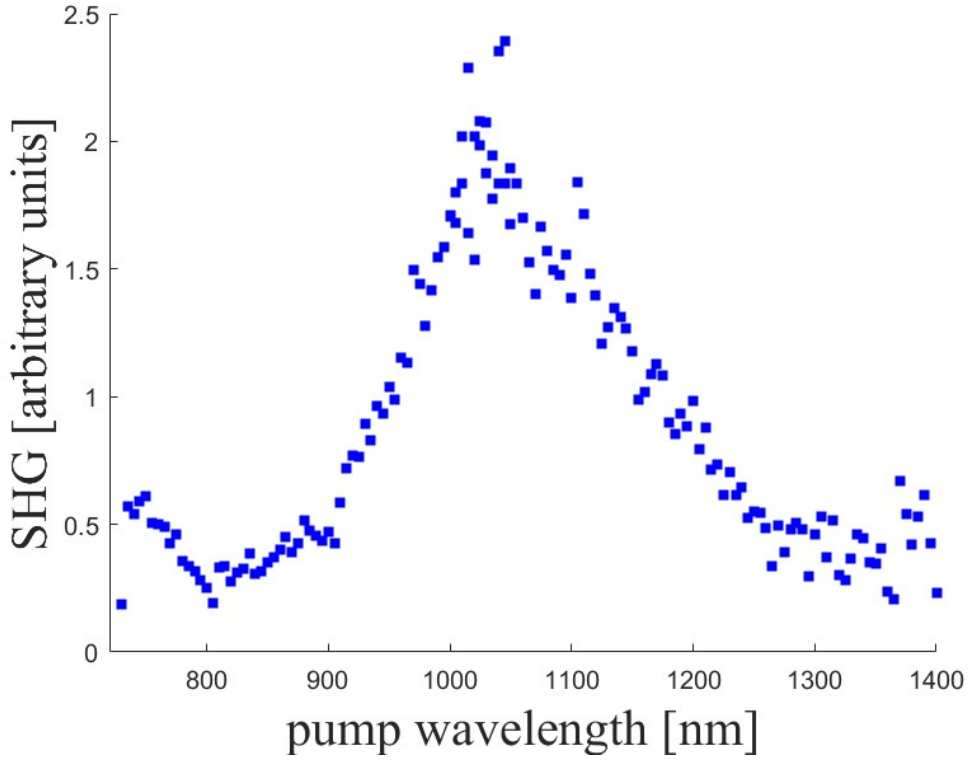

Figure 7.6: Wavelength sweep from 720 nm to 1400 nm in the *p to p* configuration. The light hits the sample at an angle of 45°. The maximum in SHG is determined to be at 1028 nm.

The dependence of the second harmonic generation at a pump wavelength of 1000 nm on the orientation of the nanowires was measured by rotating the nanorod sample described in section 6.1 around the surface normal. The polarization of the incoming light was varied between s- and p-polarization. Then, the components of the outgoing light that had the same polarization as the incoming beam and the components of the outgoing light that had the opposite polarization as the incoming beam were measured. This means the four measured configurations of the setup are *p to p*, *s to s*, *p to s* and *s to p*. The experimental results can be seen in figure 7.7. They will be compared to the predictions made by the model described in chapter 5.2. The fitting parameters for all four investigated cases can be found

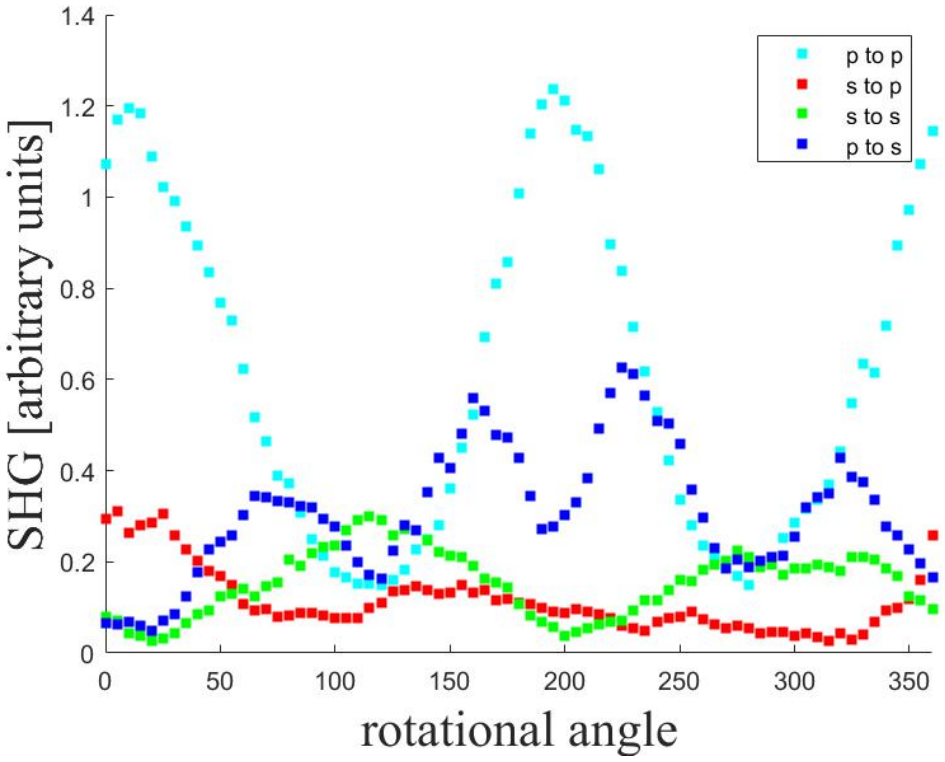

Figure 7.7: SHG for a pump wavelength of 1000 nm for all four configurations.

in table 7.1. Next to the parameters introduced in chapter 5.2, a shift in the angle ϕ - meaning along the x-axis - and a shift in the intensity - meaning along the y-axis - was also introduced to achieve a better fit to the experimental results.

Figure 7.8a shows the second harmonic generation for *p to p*. It can be seen that the maxima and minima match well between the model and the measurements, once the fitting parameters are adjusted to the data and a shift in the angle and second harmonic generation by a constant factor is implemented in the model. This is done to account for an offset in the setup for the angle and background noise for the second harmonic generation. The highest signal is measured at zero

Wavelength	A_{pp}	$B_{pp}d_{11}$	C_{pp}	$B_{ss}d_{11}$	C_{ss}	$B_{ps}d_{11}$	C_{ps}	A_{sp}	$B_{sp}d_{11}$	C_{sp}	Shift
1000 nm	0.014	1.04	0.15	0.515	0.025	1.64	0.05	0.16	0.7	0.0	-16
1200 nm	0	0.47	0.06	0.27	0	0.85	0.028	0.190	-0.194	0	-18

Table 7.1: The fitting parameters A_{pp}, A_{sp}, B_{pp}, B_{ss}, B_{ps}, B_{sp} and the shift used to fit the experimental data. Shift refers to the shift in the angle ϕ. The constants C_{ij} refers to constants being added to the overall SHG intensity.

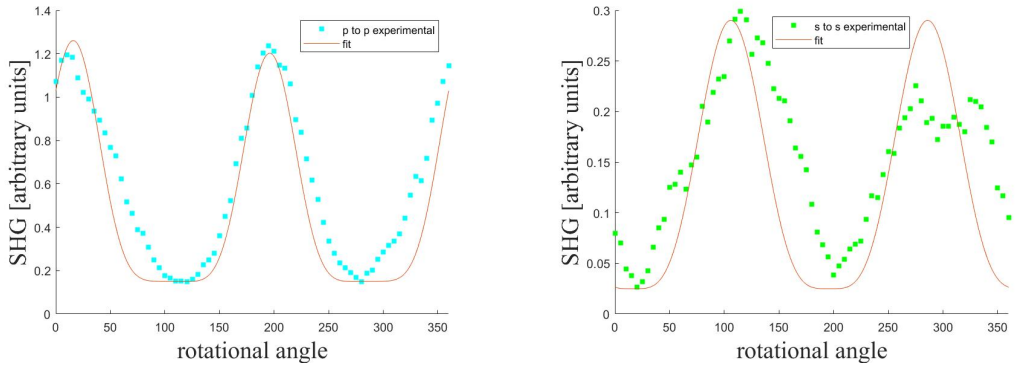

(a) *p to p* setup.

(b) *s to s* setup.

Figure 7.8: SHG for a pump wavenlength of 1000 nm in the *p to p* and *s to s* setup and the corresponding fit.

degrees where the rods are pointing down and at 180 degrees where the rods are pointing up. Here, the polarization of the incoming light is perpendicular to the rods, meaning that the present localized surface plasmon resonance is in the transversal mode. This matches with the observations from chapter 7.1.2.

The same is the case for the *s to s* polarization, which can be seen in figure 7.8b. Here, the wires are perpendicular to the direction of the polarization at approximately 90° and 270° taking the offset into account. At these angles, the highest second harmonic generation can be observed. Just like for the *p to p* case, the model gives a reliable prediction on the positions of the maxima and minima, but it should also be noted that the minima are not as broad as predicted by the model. The peaks seem to overlap, resulting in this deviation in the shape of the curve. The model does not have the necessary fitting parameters to take this into account. The broadening of the peaks might be caused by background noise. Another reason might be the experimental error caused by the misalignment of the rotational scan. Due to the near infrared wavelengths used in this experiment being invisible to the eye, precise alignment is difficult. If the spot on which the laser beam hits the sample does not coincide with the rotational axis, the spot will move on the sample and hit different inhomogeneities throughout the measurement. This will contribute to the peak broadening visible in figure 7.8b. It can also appear as intensity variations, which could explain the double peak observed around 300°.

Despite these deviations, the model explained in chapter 5.2 seems to be a fitting qualitative description of the behaviour of the second harmonic generation in relation to the orientation of the nanowires for the *s to s* and the *p to p* configurations. This supports the hypothesis from chapter 5.2 that the symmetry of the nanowire film and the array of steps described in the work of Jakobsen, Podenas and Pedersen are similar enough to use the same model to make predictions about

their second harmonic generation.

Figure 7.7 shows that for the *p to s* configuration, the maxima lay at a 45° angle compared to the maxima of the *p to p* curve. This shows that cross-polarization is present when the sample is oriented with the nanorods pointing at a 45°, 135°, 225° and 315° angle relative to the starting position, once the offset in the orientation is taken into account. The presence of these cross-polarization components support the argument from chapter 7.1 that the model calculating the reflectance would need to be extended.

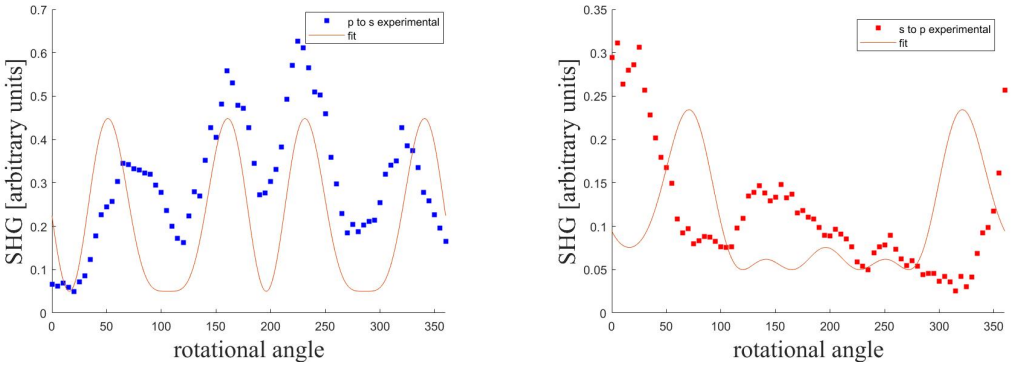

(a) *p to s* setup.

(b) *s to p* setup.

Figure 7.9: SHG for a pump wavelength of 1000 nm in the *p to s* and *s to p* setup and the corresponding fit.

From figure 7.9a, it can be seen that the wires pointing down, corresponding to the outer left and outer right peak in the plot, give a lower second harmonic generation than the wires pointing up, corresponding to the two peaks in the center of the plot. This suggests that the *p to s* configuration shows that the symmetry assumed in chapter 5.2 is broken. The model for the *p to s* case deviates more from the experimental data than for the previous two cases. Nonetheless, it exhibits the characteristic peaks. The center peaks seem to overlap, resulting in the minimum between them to not be as pronounced as the model predicts. This might be caused by background noise or imperfections in the nanocolumn film. The outer peaks are shifted towards the center in the experimental results compared to the model. Furthermore, the model predicts a constant amplitude for all four peaks, while the experimental data shows a higher second generation for the wires pointing up. As equation 5.13 can only be fitted by adjusting the amplitude, a better fit to the experimental data is not possible.

As can be seen in figure 7.9b, the experimental data for the *s to p* case exhibits a relatively weak second harmonic generation compared to the previous three configurations. The characteristic maxima and minima of the curve are covered up by the high noise to signal ratio. A maximum at zero degrees can be recognized, simi-

lar to the *p to p* case. Overall, four peaks are present in the data, with the two center peaks being strongly overlapped by the noise. Figure 7.9b furthermore shows that the results for this configuration can not be described well by the model. This could be due to the high noise to signal ratio. It could also be caused by defects in the nanostructured film having an increasing influence on the second harmonic generation with a decrease in intensity. As explained earlier in this chapter, due to misalignment in the rotational setup, these defects can look like intensity variations.

When looking at the regions of maximal cross-polarization, it becomes apparent, that the hypothesis made in chapter 5.2 does not hold. The symmetry of the layer of nanorods deviates too strongly from that of the microstructured array of steps used to develop the model. It assumes that only the d_{11} tensor element dominates the rotational dependence. Introducing other tensor elements is difficult and would require additional experimental data. Nevertheless, it can be used to make qualitative predictions about the orientations of the nanorods at which the second harmonic generation will be the strongest, as well as the overall behaviour of the second harmonic generation.

Figure 7.10 shows the second harmonic generation for the 4 different polarization cases recorded at a pump wavelength of 1200 nm. All cases exhibit lower values than their counterparts at 1000 nm. This can be attributed to the spectra being recorded further away from the peak wavelength found in the sweep, which also corresponds to the wavelength of the plasmon resonance. This effect is the most apparent for the *s to p* case, where for the 1200 nm pump wavelength, the noise becomes so dominant that the model can not be fitted to the measured data anymore. At most, it can be adjusted for the peaks to slightly coincide with those of the experimental results. For the *p to p*, the *s to s* and *p to s* case, the same characteristic behaviour can be observed for the 1200 nm pump wavelength as it is described above for the 1000 nm pump wavelength.

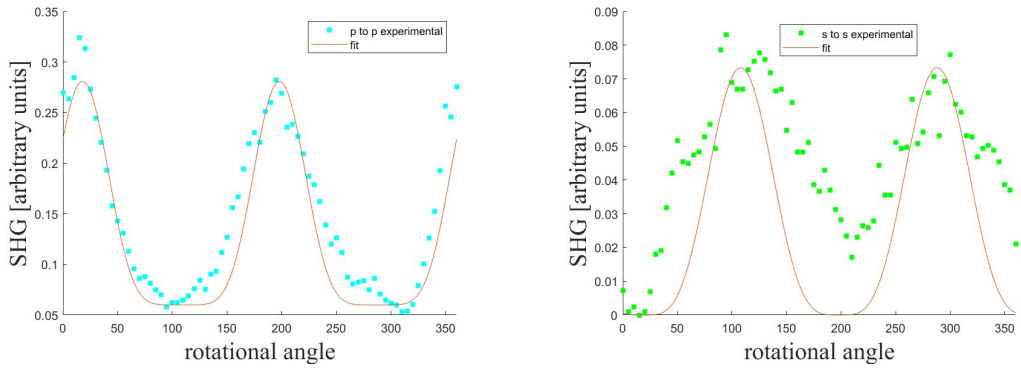

(a) p to p configuration

(b) s to s configuration

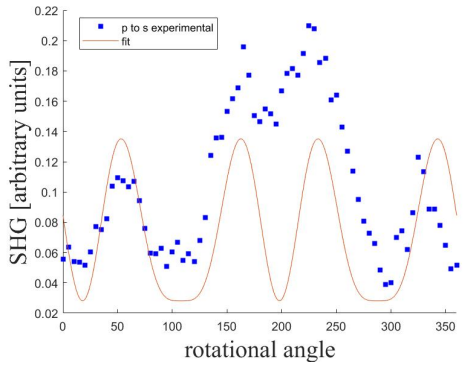

(c) p to s configuration

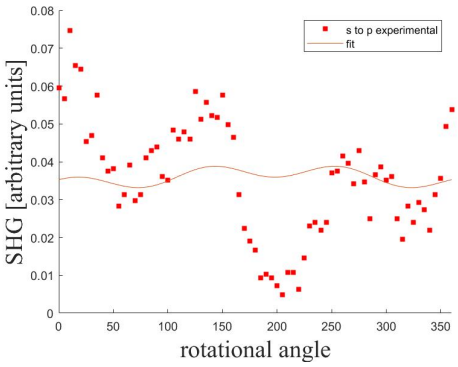

(d) s to p configuration

Figure 7.10: SHG for a pump wavelength of 1200 nm for all four configurations and the corresponding fits.

Chapter 8

Conclusion

In this thesis work, thin films with nanocolumnar gold structures were grown using glancing angle deposition. The films were deposited on silicon substrates with a 5 nm layer of chromium for increased adhesion. Their parameters such as their length and tilt angle was approximated using the scanning electron microscope.

To characterize their optical properties, two different types of optical measurements were performed on these samples. First, the linear optical properties in the form of reflectance were investigated. In order to do this, a plain gold sample was grown and measured to ensure a well working characterization process. Then, the reflectance of the nanocolumn thin film was measured. Depending on the orientation of the sample relative to the incoming light, different types of surface plasmon resonances could be observed. For the columns laying in the plane of incidence, both a bulk plasmon resonance and a localized surface plasmon resonance was observed. For the columns being rotated out of the plane of incidence, an additional surface plasmon resonance was present as well.

For both the plain gold sample and the nanocolumn sample, models were employed to make predictions about their optical behaviour. While a precise description of the experimental results was possible for the plain gold layer, the model for the nanorods needs to be further improved. While correct qualitative predictions about parts of the behaviour could be made, the influence of the three layer substrate and the rotation out of the plane of incidence were strong and could not be taken into account by the model in its present form.

The nonlinear optical properties in the form of the second harmonic generation were measured on the nanocolumn layer as well. First, a wavelength sweep was performed to determine the wavelength at which the strongest second harmonic generation can be observed. Then, four different combinations of polarizations for the incoming and outgoing light as a function of the rotation of the nanorods were measured; *p to p*, *s to s*, *s to p* and *p to s*. The strongest second harmonic generation for the case of *p to p* polarization could be observed at 0° and 180° where

the nanowires were pointing up and down, suggesting that the strongest localized surface plasmon resonance is in the transversal mode. For *p to s* polarization, cross-polarization could be observed at angles shifted by 45° relative to the *p to p* spectrum. The behaviour of the second harmonic generation on the nanocolumns was modeled using symmetry considerations from literature, which were developed for a similar structure. While this model managed to make reliable qualitative predictions for the *p to p* and *s to s* cases, for the configurations with cross-polarization, the experimental results differed strongly from the predictions made by the model. This suggests a strong difference between the symmetry of the investigated sample and the symmetry of the structure modeled in the paper. The measurements themselves were affected by misalignment of the laser beam. Due to the beam not being aligned along the optical axis of the sample, it moved on the surface during the rotational measurement, causing it to hit different defects throughout the measurements. These defects appear in the spectra as variations in intensity and cause peak broadening.

The linear and nonlinear optical properties of thin films with gold nanorods were thoroughly measured and analysed in this work. They showed a strong dependence on the polarization and angle of the incoming light, as well as the orientation of the rods in relation to the plane of incidence of the incoming light, proving glancing angle deposition to be a powerful tool for the engineering of optical properties of thin films.

Chapter 9

Outlook

To further investigate the optical behaviour of the nanostructured films grown in this work, more measurements should be done. The effect of the polarization of the incoming light on the reflectance should be investigated. In order to do this, the measurements discussed in chapter 7.1 should be repeated with s-polarized light. Since the light used to measure the reflectance hits the substrate at a nearly orthogonal angle, it is reasonable to expect that for s-polarized light, the reflectance looks as if the sample was rotated by 90°. Since this is not the case according to the model used to predict the reflectance, the behaviour of the sample with s-polarized light should be investigated experimentally.

The model for the reflectance of the nanorod film itself can be further improved as well. First, a three layered substrate should be implemented with a semi-infinite silicon layer in the bottom, followed by a 5 nm chromium layer and a thin gold layer on top. Like this, the model should be able to take the different characteristic influences of the different components of the substrate, which became apparent in chapter 7.1.2, into account. Furthermore, when the sample is rotated out of the plane of incidence, the model is no longer valid, leading to strong deviations between the predictions it can make for the rotated sample and the experimental results. Therefore, to improve the model such that predictions about the reflectance can be made for all four measured orientations of the nanorods, these rotations of the substrate coordinate system around the surface normal should be added.

Apart from further analysing the properties of the films grown in this work, the quality of the structure itself can also be increased. For this, the homogeneity and regularity of the nanorods should be improved. One approach to improve the regularity of the columns is a technique called seeding. Here, instead of letting the nuclei at which the columns start to grow be distributed randomly on the surface at the beginning of the deposition, nuclei are introduced to the substrate surface in an ordered pattern and with a regulated size before the deposition. The seeds can for example be created using e-beam lithography [16]. It was attempted to

create a seeding pattern using this method, but due to limitations of the available equipment, it did not succeed. For nanocolumns of the dimensions as they were grown in this work, seeds around 50 nm in height and diameter should be grown with a distance of around 600 nm between them [16]. As the available scanning electron microscope used to attempt the creation of a seeding pattern is commonly used to develop line and area e-beam patterns, the beam blanker was not adjusted properly to be able to write a point pattern. This resulted in the area between the points being exposed as well. The adjustments to fix this problem could not be made in time. Implementing a seeding pattern in the fabrication process would significantly increase the regularity of the films, as it would prevent column extinction. This would improve the optical properties, as it would reduce the influence of defects and irregularities on the measurements.

Another factor contributing to the irregularites of the films was the substrate with 5 nm of chromium on top. They were cleaned before they were deposited on. Nevertheless, irregularities in the film could be observed. This is most likely due to contamination of the silicon that is trapped under the chromium layer. These irregularities then function in a similar way to the seeds, but in a non-ordered way, decreasing the regularity and thus the quality of the grown nanorods. Therefore, the preparation of the substrates should be optimized.

A more regular nanocolumn film could be described more accurately in the theoretical model. As is mentioned in chapter 7.1, the film parameters such as length or distance of the columns have a strong influence on the predictions the model makes, but the model can not take irregularities in these parameters into account. By making the columns and the distance between them more regular, the behaviour of the film would become more easy to model. Reducing the column extinction and the material deposited between the singular columns might also make it possible to model the substrate as only having two layers, 5 nm of chromium and a semi-infinite silicon layer.

The nonlinear measurements can be improved by developing a more reliable way to align the sample. A beam at wavelengths visible to the eye could be added during the alignment process, such that the spot on which the laser beam hits the sample can more easily be aligned with the rotational axis. This would decrease the influence of inhomogeneities on the measurements and thereby also the peak broadening. Furthermore, more measurements per configuration should be made to achieve more statistically significant results. The model used to make predictions for the second harmonic generation of the samples can be improved as well. It was developed for a structure with a similar, but not identical symmetry. The model assumes that all the tensor elements besides d_{11} can be neglected. Investigating the symmetry of the sample grown and measured in this thesis work and introducing other tensor elements to the model could improve it significantly.

Bibliography

[1] Mohsin Ali Badshah et al. "Enhancing the Sensitivity of a Surface Plasmon Resonance Sensor with Glancing Angle Deposited Nanostructures". In: *Plasmonics* 15 (Dec. 2020), pp. 1–4, 6.

[2] Angel Barranco et al. "Perspectives on oblique angle deposition of thin films: From fundamentals to devices". In: *Progress in Materials Science* 76 (2016), pp. 61–79, 127–128.

[3] Robert W Boyd. *Nonlinear optics*. third. Academic press, 2008, pp. 1–6, 40, 44–46.

[4] Wenshan Cai, Vladimir Shalaev, and Dilip Paul. "Optical Metamaterials: Fundamentals and Applications". In: *Physics Today - PHYS TODAY* 63 (Sept. 2010), pp. 1–3, 19–24.

[5] Tasnim Gharbi et al. "Fitting optical properties of metals by Drude-Lorentz and partial-fraction models in the [0.5; 6] eV range". In: *Optical Materials Express* 10.5 (2020), pp. 1129–1162.

[6] Matthew M Hawkeye, Michael T Taschuk, and Michael J Brett. *Glancing angle deposition of thin films: engineering the nanoscale*. First Edition. John Wiley & Sons, 2014, pp. 41–46, 53–59, 128–133.

[7] U. Hohenester. *Nano and Quantum Optics: An Introduction to Basic Principles and Theory*. Graduate Texts in Physics. Springer International Publishing, 2019, p. 83.

[8] C. Jakobsen, D. Podenas, and K. Pedersen. "Optical second-harmonic generation from vicinal Al(100) crystals". In: *Surface Science* 321.1 (1994), pp. 1–3.

[9] PB Johnson and RW Christy. "Optical constants of transition metals: Ti, v, cr, mn, fe, co, ni, and pd". In: *Physical review B* 9.12 (1974), p. 5056.

[10] Peter B Johnson and R-WJPrB Christy. "Optical constants of the noble metals". In: *Physical review B* 6.12 (1972), p. 4370.

[11] A Knoesen, MG Moharam, and TK Gaylord. "Electromagnetic propagation at interfaces and in waveguides in uniaxial crystals: surface impedance/admittance approach". In: *Applied Physics B* 38 (1985), pp. 171–178.

[12] J.D. Musgraves, J. Hu, and L. Calvez. *Springer Handbook of Glass*. Springer Handbooks. Springer International Publishing, 2019, pp. 1294–1295.

[13] Lukas Novotny and Bert Hecht. *Principles of nano-optics*. second. Cambridge university press, 2012, pp. 369–370.

[14] Frank L Pedrotti, Leno M Pedrotti, and Leno S Pedrotti. *Introduction to optics*. Third Edition. Cambridge University Press, 2017, pp. 491–497, 539, 371.

[15] GB Smith. "Effective medium theory and angular dispersion of optical constants in films with oblique columnar structure". In: *Optics Communications* 71.5 (1989), pp. 279–284.

[16] Michael T. Taschuk, Matthew M. Hawkeye, and Michael J. Brett. "Chapter 13 - Glancing Angle Deposition". In: *Handbook of Deposition Technologies for Films and Coatings (Third Edition)*. Ed. by Peter M. Martin. Third Edition. Boston: William Andrew Publishing, 2010, pp. 621–678.

[17] Sammy Verbruggen et al. "Predicting the Surface Plasmon Resonance Wavelength of Gold–Silver Alloy Nanoparticles". In: *The Journal of Physical Chemistry C* 117 (Aug. 2013), p. 1.

[18] Yanfeng Wang, Zhengjun Zhang, and Yiping Zhao. "The IR plasmonic properties of sub-wavelength ITO rod arrays predicted by anisotropic effective medium theory". In: *Nanotechnology* 31.7 (2019), pp. 1–10.